Supporting Information

Formation of Bismuth Nanosheets on Copper Foam Coupled with Nanobubble Technology for Enhanced Electrocatalytic CO_2 Reduction

Kai Wu [a, b], Pengwei Yang [a, b], Shuaijun Fan [a, b], Yifan Wu[b], Jingxiang Ma [a, b], Lijuan Yang[b], Hongtao Zhu[b], Xiaoying Ma[b], Heli Gao[c], Wentong Chen[c], Jun Jia[c], Shuangchen Ma *[, a, b]

a MOE Key Laboratory of Resources and Environmental Systems Optimization, School of Environmental Science and Engineering, North China Electric Power University, Beijing, 102206, PR China.

b Hebei Key Laboratory of Power Plant Flue Gas Multi-Pollutants Control, Department of Environmental Science and Engineering, North China Electric Power University, Baoding, 071003, PR China.

c Shenzhen Energy Baoding Power Co., Ltd, Baoding, 072150, PR China.

*Corresponding author. Email address: msc1225@163.com (Shuangchen Ma).

Section S1. Materials and apparatus

Materials

Bismuth chloride ($BiCl_3$, 99%) and potassium bicarbonate ($KHCO_3$, >99.5%) were purchased from Aladdin (Shanghai, China). Dimethyl sulfoxide (DMSO, >99%), hydrochloric acid (HCl, 37%), acetone (>99.5%) and ethyl alcohol (EtOH, >99.5%) were purchased from Kermel (Tianjin, China). Carbon black (xc-72R, 10-20 nm), polyvinylidene fluoride (average Mw ~ 534000, powder) were purchased from Macklin (Shanghai, China). Copper foam (99.9%, 110 PPI) was purchased from Keshenghe technology Co., Ltd (Suzhou, China). Bismuth plate (1*10*10 mm, 99.9%) was purchased from Tengfeng metal materials Co., Ltd (Xingtai, China). Carbon paper (HCP020P, hydrophobic) purchased from Suzhou Shengernuo Technology Co., Ltd. CO_2 (99.9%) and N_2(99.9%) were purchased from Huawei Gas technology Co., Ltd (Baoding, China). The ultrapure water (18.4 MΩ cm) was prepared by a reverse osmosis high purity water machine (Xinjia environmental protection special equipment manufacturing Co. Ltd., Baoding, China).

Apparatus

X-ray diffraction (XRD) data were collected on a Bruker D8 ADVANCE instrument. Transmission electron microscopic (TEM) images were collected on a JEOL Jem-2100F instrument. Scanning electron microscopic (SEM) images were collected on a Thermo Fisher Quattro S instrument. Energy-dispersive X-ray spectroscopy (EDS) data were collected on a EDAX ELECT PIUS instrument. Atomic force microscopy (AFM) image was captured by Bruker Dimension icon XR in contact mode. X-ray photoelectron spectroscopy (XPS) data were collected on a Thermo Fisher Nexsa instrument. The particle size and zeta potential of CO_2 bubbles in the electrolyte were determined with Zetasizer Nano ZS90 (Malvern, UK). The number concentration of CO_2 bubbles in the electrolyte was measured with Zetaview-PMX120-Z (Particle Metrix, Germany). Formate concentration data were collected by SHIMADZU LC-20A high-performance liquid chromatograph. The electrochemical characteristics data were collected by DH 7000D electrochemistry workstation (Jiangsu Donghua Analytical Instrument Co., Ltd.). CO_2 nanobubbles were produced from ZJC-NM-200L nanobubble generator (Shanghai Zhongjing Environmental Protection Technology Co., Ltd.).

Section S2. Experimental section

Synthesis method

Synthesis of Bi/CF

A piece of Cu foam was washed with acetone, transferred to 0.5 M HCl solution, ultrasonicated for 10 min, and rinsed with water and ethanol. The cleaned Cu foam was then immersed in dimethyl sulfoxide (DMSO) solution containing 0.01 M $BiCl_3$ and 0.1 M HCl. The color of the Cu foam immediately changed from burgundy to dark brown. After 5 min, the Cu foam was removed from the solution and rinsed with water and ethanol. The obtained Bi coated Cu foam was dried under N_2 gas flow at room temperature and denoted as Bi/CF.

Synthesis of Bi_2O_3/CF and Bi NSs/CF

The prepared Bi/CF was placed in a tube furnace and annealed at 200 ℃ for 2 hours in an air atmosphere, with a heating rate of 2 ℃·min^{-1}. After naturally cooling the tube furnace to room temperature, the sample was retrieved and denoted as Bi_2O_3/CF. Subsequently, Bi_2O_3/CF was installed as the cathode (working electrode) in a single electrolysis cell. In a CO_2-saturated 0.5 M $KHCO_3$ electrolyte, the working electrode underwent 20 cycles of cyclic voltammetry scans at a scan rate of 20 mV·s^{-1} under a potential range of -0.2 to -1.2 V vs. RHE. This process ultimately produced copper foam coated with bismuth nanosheets, denoted as Bi NSs/CF.

Evaluation of catalyst performance

The performance evaluation of the materials were carried out using a typical H-type cell with a three-electrode system, in which the anode and cathode reaction cells were separated by a proton exchange membrane (N117, Dupont). The electrolyte was composed of 0.5 mol·L^{-1} $KHCO_3$ solution, with Bi plate, Bi/CF or Bi NSs/CF as the working electrode (cathode), Ag/AgCl (saturated with KCl) as the reference electrode, and 0.2×10×10 mm platinum plate as the counter electrode (anode). Potentials while measured vs Ag/AgCl (saturated with KCl) are converted to the RHE scale using the formula: E (vs. RHE) = E (vs. Ag/AgCl) + 0.197 V + 0.0591 V × pH. All electrochemical experiments were performed at room temperature (22 ± 1 ℃). High-purity CO_2 was passed into the electrolyte to saturation (50 mL·min^{-1} for 30 min) before the experiment, and CO_2 was continuously supplied to the electrolyte (50 mL·min^{-1}) during the experiment. Notably, when experiments were conducted using an H-type cell that combines nanobubble technology with a flowing electrolyte, an intermittent CO_2 supply method was employed. Specifically, a nanobubble generator was integrated into the electrocatalytic system, operating for 5 minutes every hour during the experiment to produce an electrolyte rich in nano-sized CO_2 bubbles. The electrolyte volume was 400 mL, and the CO_2 flow rate was 800 mL·min^{-1}. The potentials applied during bulk electrolysis were selected on the basis of voltammetric data obtained under the same conditions. Upon completion of the electrolysis, a syringe was employed to

extract a portion of the electrolyte, which was subsequently subjected to filtration through a 4.5 μm filter head. The filtered solution was then transferred into a vial and sealed for preservation, in preparation for its utilization in high-performance liquid chromatography (HPLC) analysis.

Analysis of the electrolysis products

The concentration of formate products was detected by SHIMADZU LC-20A high-performance liquid chromatograph. The chromatographic column was AQ-C18 (5 um, 4.6×250 mm, Dalian Ilitar Supersil). The eluting method was binary high-pressure gradient elution, mobile phase A was CH_3OH, mobile phase B was 0.05 mol·L^{-1} KH_2PO_4 (pH = 2.7), and the flow rates of mobile phase A and B were controlled to be 3% and 97% respectively to form buffer solution (volume fraction). The flow rate was 0.5 mL·min^{-1} at room temperature. The detection wavelength was 215 nm, and the injection volume was 20 uL. Before injection, phosphoric acid was used to adjust the pH of the sample to 2.7. In this method, the characteristic peak of formate appears around 7.2 minutes. The standard curve for formic acid is illustrated in Figure S1, and its corresponding data is provided in Table S1.

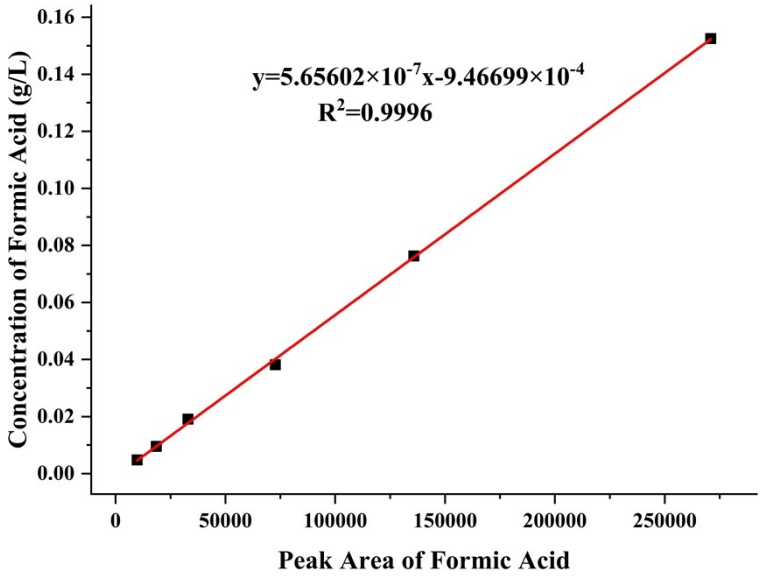

Figure S1. Standard curve of formate.

Table S1. Data relating to the standard curve for formic acid.

Component	Linear range (g L^{-1})	Linear equation	Coefficient of association
Formate	0.00476563~0.1525	$y=5.65602\times10^{-7}x-9.46699\times10^{-4}$	0.9996

Note:

y, the mass concentration of formate, g L^{-1}.

x, peak area of formate.

Calculation of faradaic efficiency, cathodic energy efficiency and CO_2 conversion rate

The faraday efficiency of formate in liquid products was determined as follows:

$$FE_{Formate}(\%) = \frac{Q_{Formate}}{Q_{Total}} \times 100\% = \frac{n \times N_{Formate} \times F}{I \times t} \times 100\%$$

Where, $Q_{Formate}$ is the amount of electricity needed to produce formate, C.

Q_{Total} is the electricity consumed by the entire electrochemical process, C.

n is the number of electrons transferred from a molecule of CO_2 to a molecule of formate, and since C in CO_2 has a +4 valence, and C in formate has a +2 valence, so n is 2.

$N_{Formate}$ is the molar mass of formate in the liquid phase product, mol.

F is Faraday constant, F=96485 C·mol^{-1}.

I is the current, A.

t is time, s.

The cathodic energy efficiency can be calculated as follows[1-3]:

$$EE_{Formate}(\%) = \frac{E_{Water}^{0} - E_{Formate}^{0}}{E_{Water}^{0} - E_{Applied}} \times FE_{Formate} \times 100\%$$

Where, E_{Water}^{0} represents the standard water oxidation potential, here taken as 1.23 V.

$E_{Formate}^{0}$ represents the standard electrode potential for formate production, here taken as -0.20 V.

$E_{Applied}$ is the applied potential, V.

$EE_{Formate}$ is the cathodic energy efficiency of formate production, %.

The CO_2 conversion rate was calculated as follows:

$$CO_2\ conversion\ rate(\%) = \frac{N_{Formate}}{N_{CO_2}} \times 100\%$$

Where, N_{CO2} is the CO_2 molar flow rate at the inlet of the cathode chamber, mol. Here, due to the differences in CO_2 gas supply forms, the CO_2 supply amount was normalized, as detailed in Table S3.

DFT calculations

Spin-unrestricted first-principles calculations were performed using the Dmol3 software package[4]. The Perdew-Burke-Ernzerhof (PBE) generalized gradient approximation (GGA) was employed to approximate the exchange-correlation functional. The double numerical polarization (DNP) basis set and DFT semicore pseudopotentials (DSPP) were utilized to accurately describe the core and valence electrons, respectively. A truncation radius of 5.0 Å was employed, and the convergence criteria for all geometry optimizations were set as an energy difference of 1.0×10^{-5} Ha (where 1 Ha = 27.2114 eV) between adjacent structures, a maximum force of 0.002 Ha/Å per atom, and a maximum displacement of 0.005 Å. The standard unit cells of Bi and Cu were obtained from the ICSD database[5]. After structural optimization, the unit cells were sliced to expose the (0 1 2) crystal plane of Bi (a=4.7657 Å, b=4.9426 Å) and the (1 1 1) crystal plane of Cu (a=8.7052 Å, b=5.0260 Å). Subsequently, the (0 1 2) crystal plane of Bi and the (1 1 1) crystal plane of Cu underwent 2×2 and 1×2 supercell treatments(Bi(0 1 2)-layer: a= 9.5314 Å, b= 9.8852

Å; Cu(1 1 1)-layer: a= 8.7052 Å, b= 10.0519 Å), respectively, to facilitate the construction of the Bi/Cu heterojunction. Two layers of Bi(0 1 2)-layer were stacked on two layers of Cu(1 1 1)-layer, and a vacuum layer of 15 Å was established along the z-axis, resulting in the Bi(0 1 2)/Cu(1 1 1) configuration. The lattice mismatch rate in the a direction is 9.5314-8.7052/9.5314*100%=8.6678%, and in the b direction, it is 10.0519-9.8852/10.0519*100%=1.6583%, both of which are less than 10%. The Bi(0 1 2)/Cu(1 1 1)-Defect model was constructed based on the Bi(0 1 2)/Cu(1 1 1) configuration by removing some Cu atoms from the third layer. The Bi(0 1 2) model was composed of four layers of Bi(0 1 2)-layer stacked together. All configurations were structurally optimized. During geometry optimization and electronic performance calculations, Monkhorst-Pack k-points were chosen as 3×3×1 in the first Brillouin zone. Solvent models were not considered in this study.

The reaction steps for electrochemical reduction of CO_2 to formic acid (equation 1~2), CO (equation 3~4) and competing HER (equation 5~6) are as follows:

$$*+ CO_2 + H^+ + e^- = *OCHO \quad (1)$$

$$*OCHO + H^+ + e^- = *+ HCOOH \quad (2)$$

$$*+ CO_2 + H^+ + e^- = *COOH \quad (3)$$

$$*COOH + H^+ + e^- = *+ CO + H_2O \quad (4)$$

$$*+ H^+ + e^- = *H \quad (5)$$

$$*H + H^+ + e^- = *+ H_2 \quad (6)$$

where * is the adsorption site, *H, *OCHO and *COOH are the reaction intermediates, respectively. The Gibbs free energy G of the computational model is defined as[6]:

$$G = E_{DFT} + E_{ZPE} + \int C_P dT - TS \quad (7)$$

where E_{DFT}, E_{ZPE}, Cp and S are the electronic energy, zero-point energy, heat capacity and entropy, respectively. For adsorption intermediates, E_{ZPE}, S and Cp were determined by vibrational frequency calculations via standard methods. The calculations were all performed using the computational hydrogen electrode (CHE) model, which assumes that the free energy of protonation of H_2 is zero under standard conditions. The electron energy (E_{DFT}), zero-point energy correction (E_{ZPE}), heat capacity and entropy contributions (∫CpdT-TS) in this study are shown in Table S4. The free energy changes (ΔG) of the reaction paths in this study are shown in Table S5.

Section S3. Supplementary figures and tables

Copper foams were immersed in a DMSO solution containing 0.01 M $BiCl_3$ and 0.1 M HCl to investigate the effect of the duration of Bi^{3+}/Cu galvanic replacement on the Cu/Bi composition ratio and physical stability of the materials.

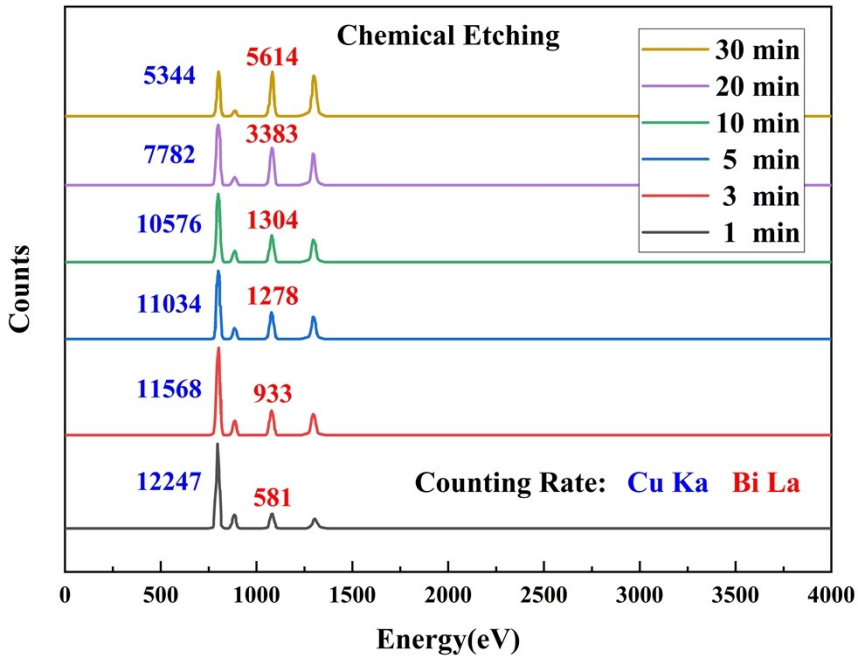

Figure S2. The operation time of Bi chemical etching instead of Cu directly affects the proportion of Cu/Bi components in the material.

The results showed that as the duration of the Bi chemical etching of Cu extended, the content of Bi in the material initially exhibited a rapid increase (from 1 to 5 minute, indicated by the black, red and blue lines in Figure S2), suggesting that the Cu were quickly chemically substituted by Bi. Subsequently, the Bi content in the material stabilized (from 5 to 10 minutes, shown by the blue and green lines in Figure S2), indicating that after 5 minutes of chemical etching, the Cu foam surface had achieved near-complete coverage with a Bi coating. At this point, the reduction in the Cu surface area slowed down the Bi loading process. However, during this period, the formed Bi coating would slowly react with HCl in the solution, regenerating BiCl3, which then dissolved back into the solution. This triggered a chain etching reaction involving the "slow dissolution of the Bi coating," followed by the "exposure of fresh Cu surfaces," and subsequently the "reformation of the Bi coating." As the operation time was extended further (from 10 to 30 minutes, indicated by the green, purple and yellow lines in Figure S2), Bi etching gradually penetrated deeper into the interior of the Cu foam, which was evidenced by a significant change in the Cu/Bi compositional ratio within the material.

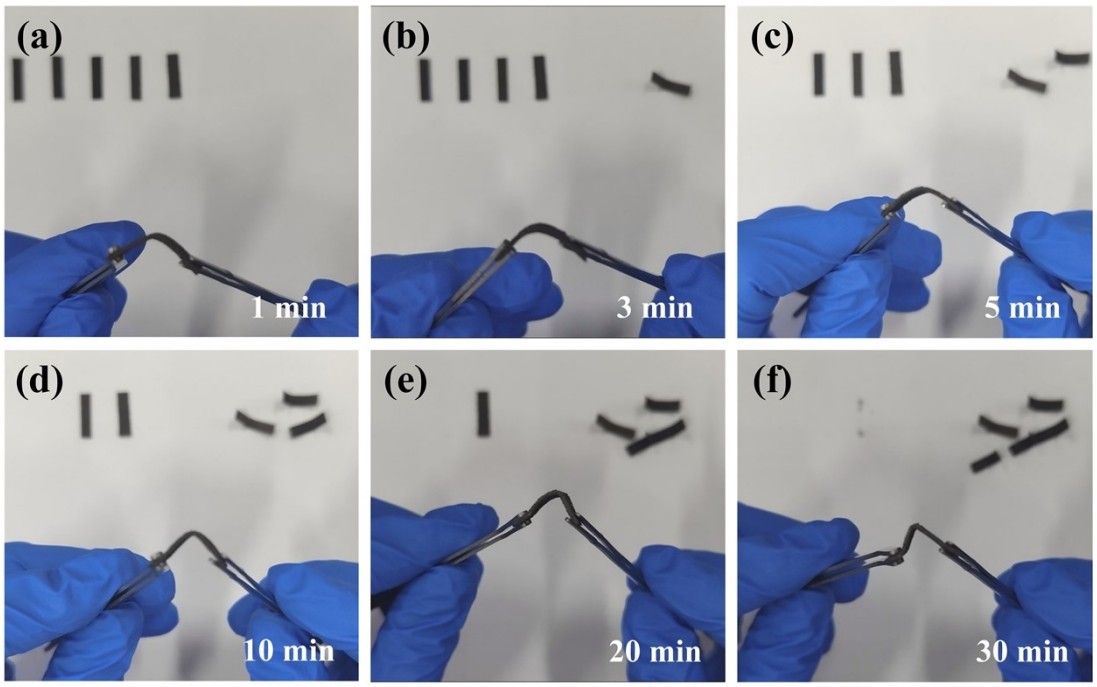

Figure S3. The operation time of Bi chemical etching instead of Cu is directly related to the physical structure stability of the material.

As the experimental results showed, prolonged etching led to the complete replacement of the Cu skeleton by Bi, reducing the material's mechanical properties. Such an outcome is detrimental for its use as an electrode, as it would decrease the electrode's lifespan in long-term electrochemical activities.

In summary, to achieve near-complete coverage of the Cu foam surface with a Bi coating while ensuring sufficient physical structural stability, a 5-minute operation time was determined as the optimal duration for the Bi^{3+}/Cu galvanic replacement process in a DMSO solution containing 0.01 M $BiCl_3$ and 0.1 M HCl.

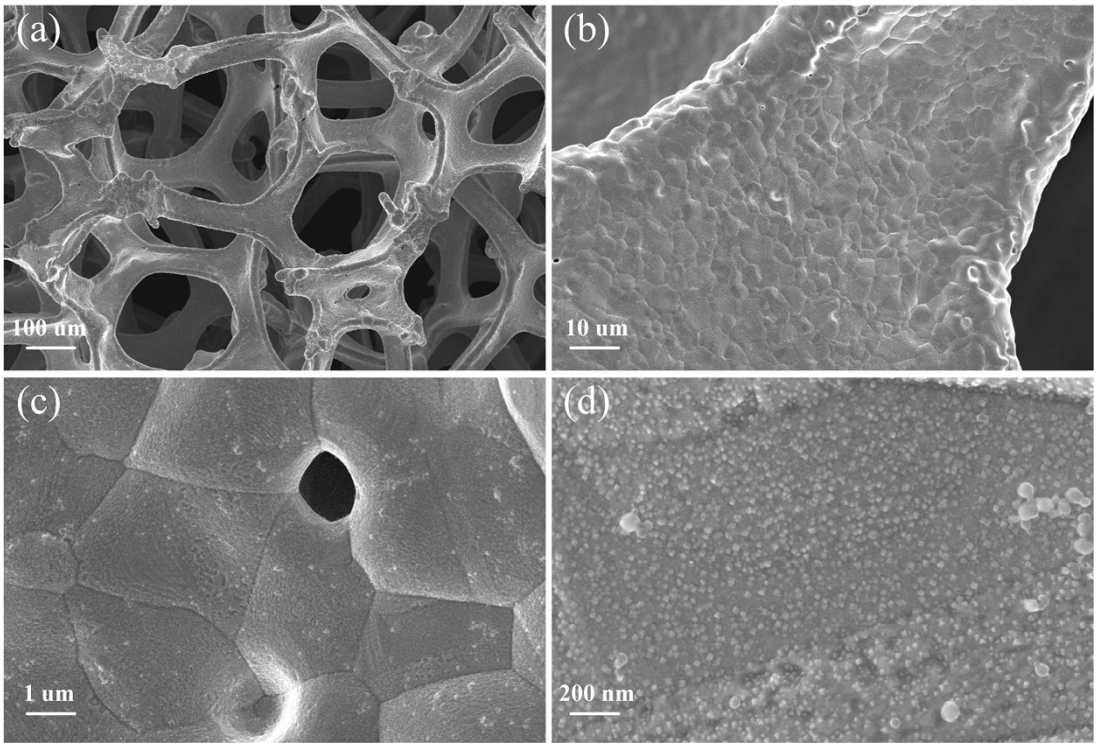

Figure S4. SEM images of Cu foam.

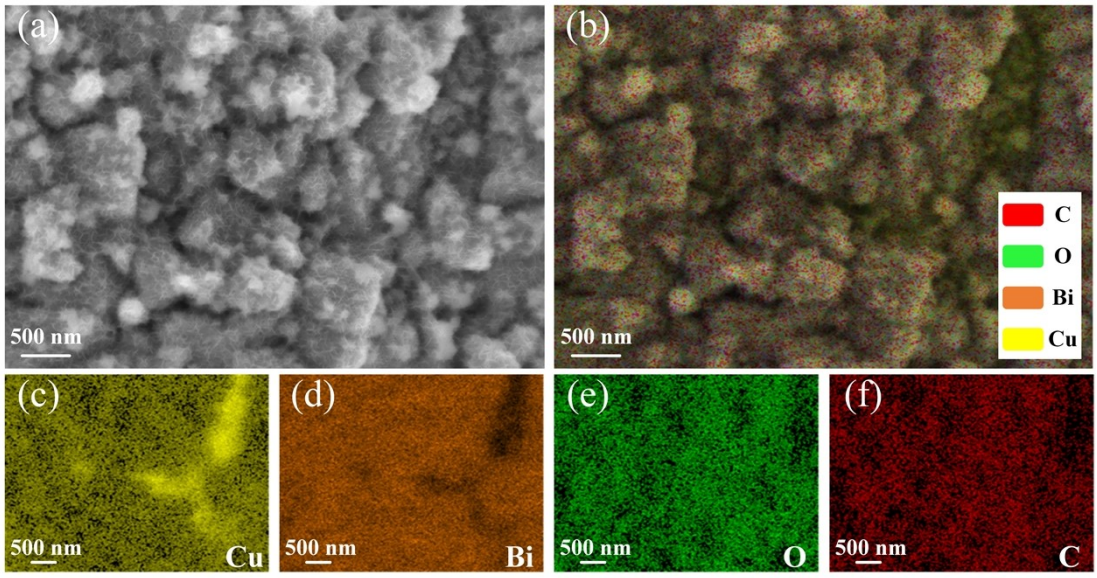

224

225 Figure S5. (a) SEM image of Bi NSs/CF. (b-f) SEM EDS mapping images of Bi NSs/CF.

226

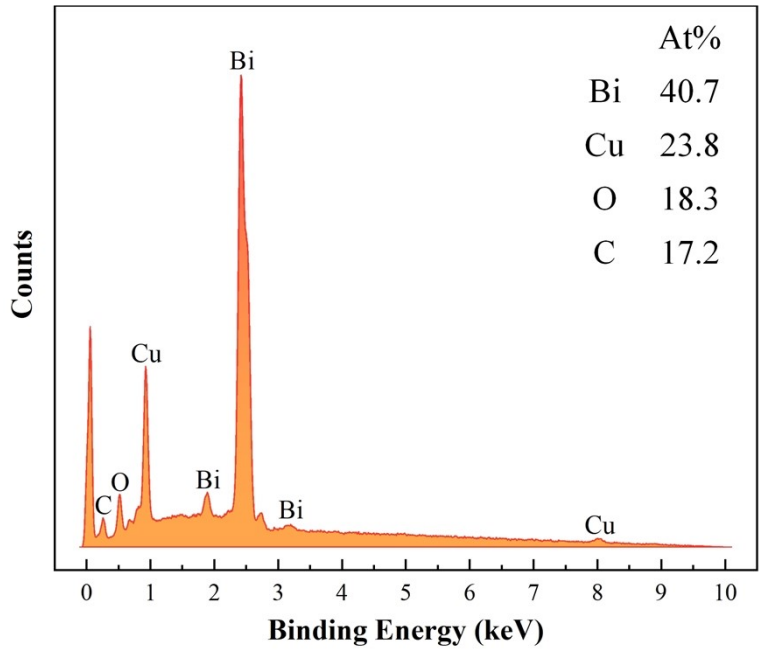

227

228 Figure S6.SEM EDS pattern of Bi NSs/CF and corresponding semi-quantitative results.

229

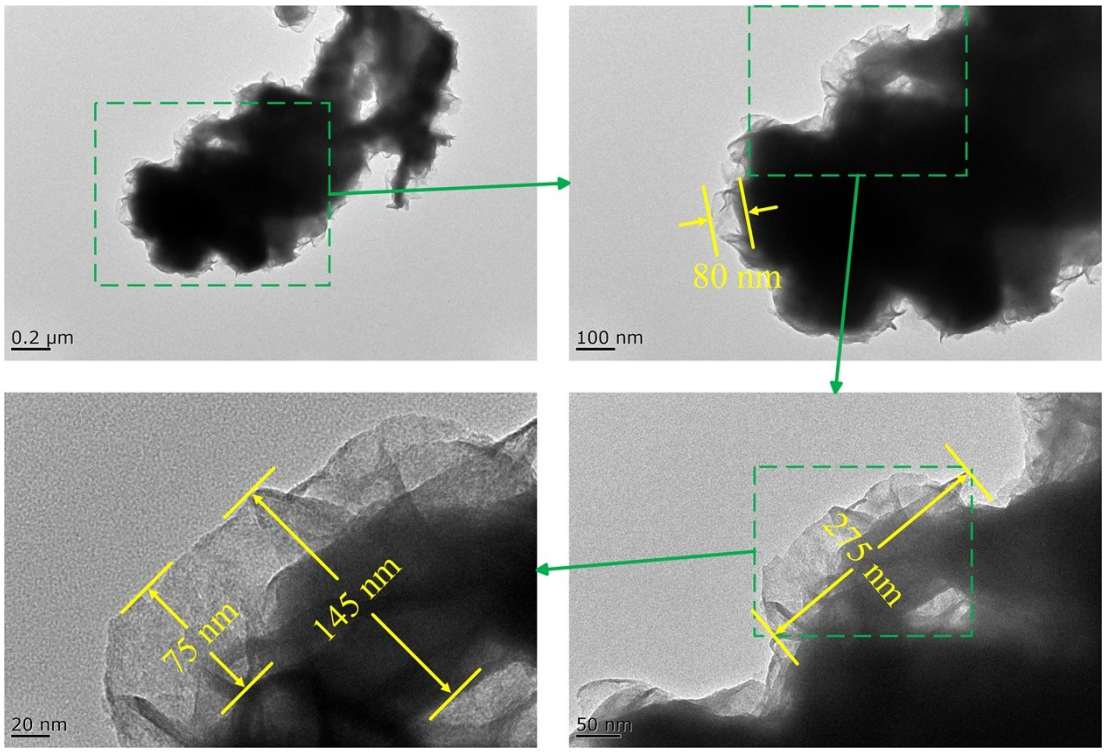

Figure S7. TEM images of Bi NSs with corresponding dimensional measurements.

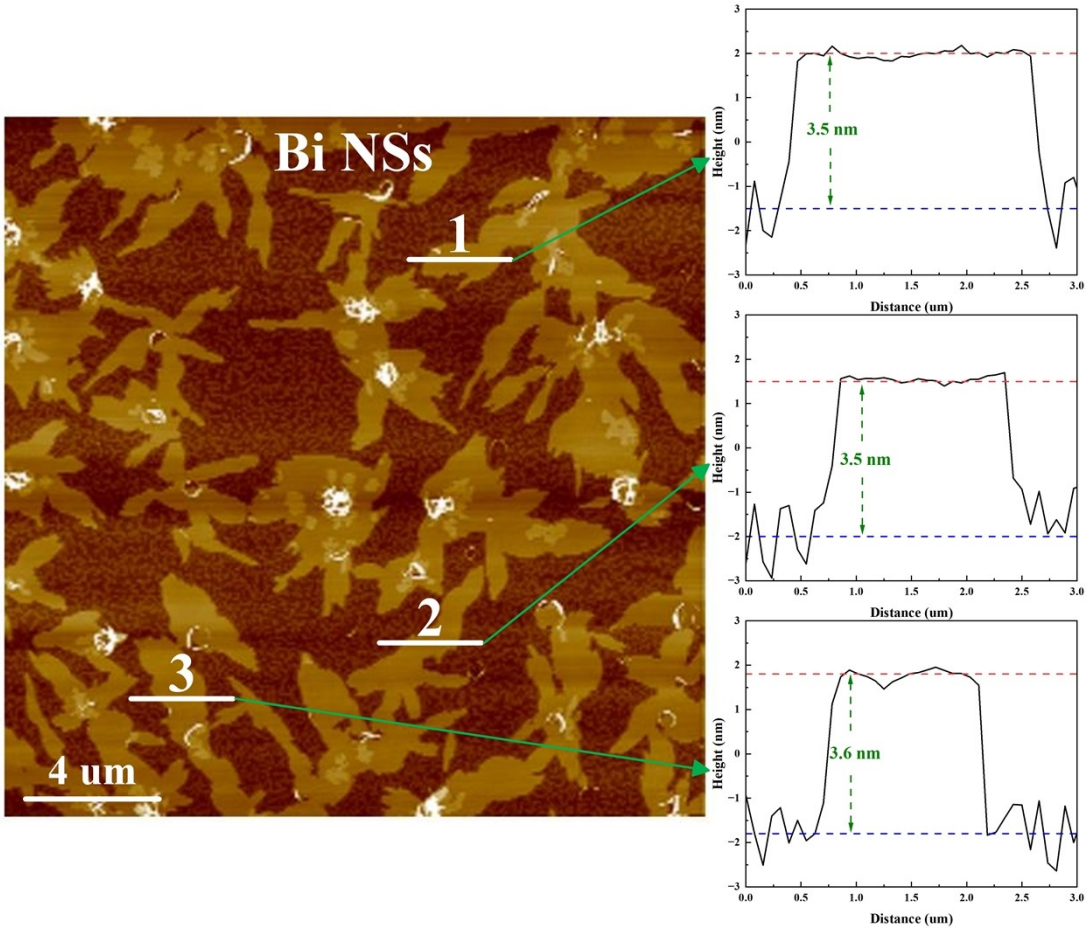

Figure S8. AFM image of Bi NSs with corresponding thickness labeling.

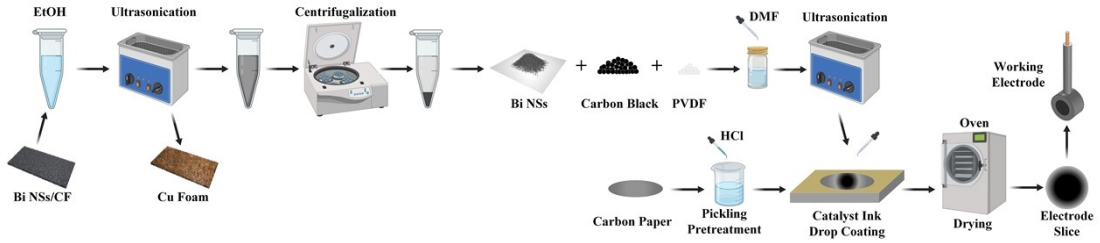

Figure S9. Flow chart for preparation of Bi NSs/CP electrode.

To evaluate the CO_2RR characteristics of Bi NSs, we stripped the Bi NSs from the Bi NSs/CF material and loaded them onto carbon paper (CP) to form the Bi NSs/CP electrode, which was tested in an H-type cell equipped with a three-electrode system.

The specific preparation process of the Bi NSs/CP electrode is illustrated in Figure S9. Initially, the Bi NSs/CF material was placed in an ethanol solution and ultrasonicated for 30 minutes to strip the Bi NSs from the surface of the material into the solution. Afterwards, clean ceramic tweezers were used to remove the Cu foam stripped of Bi NSs from the solution, and the ethanol solution containing the Bi NSs was transferred to a centrifuge tube and centrifuged at 5000 rpm for 10 minutes. The supernatant was discarded, and the resultant grey black Bi NSs material was dried in an oven at 70 ℃ for 1 hour and collected for further use. Next, the Bi NSs, carbon black, and polyvinylidene fluoride (PVDF) were mixed in a mass ratio of 8:1:1 and added to a 10 ml vial. A certain amount of DMF was added to wet and dissolve the mixture (equivalent to 0.1 g of solid material combined with 1 ml of DMF). The vial was then placed in an ultrasonic bath and sonicated at room temperature for 30 minutes to obtain a uniformly dispersed catalyst ink. A specific volume of this catalyst ink was evenly drop-cast onto pre-treated carbon paper (50 μl of catalyst ink drop-cast onto a circular carbon paper with a diameter of 5.5 mm, effective electrode area of 0.94985 cm^2). The coated carbon paper was air-dried at room temperature for 30 minutes to promote initial solidification of the catalyst ink. The sample was then transferred to an oven at 70 ℃ and dried for 1 hour to obtain the electrode sheet. The electrode sheet was fixed in an electrode holder to form the working electrode.

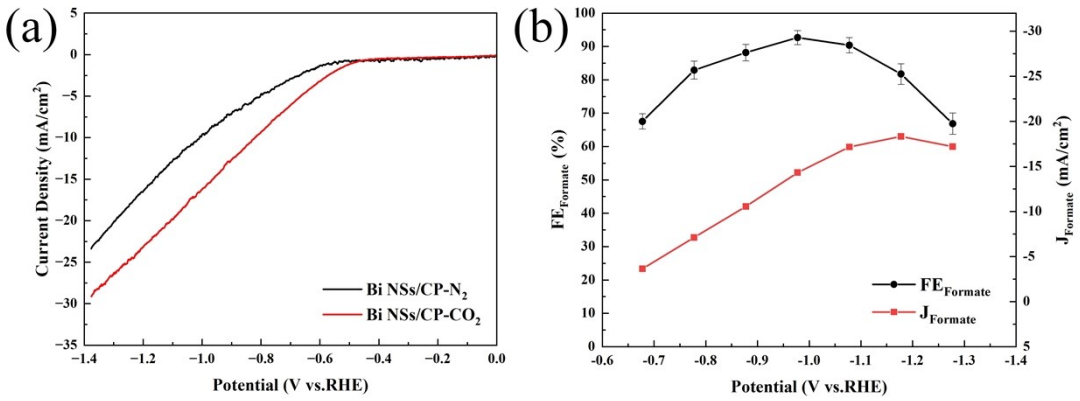

Figure S10. CO_2RR performance of Bi NSs/CP.

(a) LSV curves in N_2 or CO_2 atmosphere. (b) Faradaic efficiencies and partial current densities of formate.

The results indicated that in terms of formate selectivity, the Bi NSs/CP electrode performed at a similar level to the Bi NSs/CF electrode, suggesting that the Bi NSs were the source of this excellent CO_2RR activity. However, the total current density achieved with the Bi NSs/CP electrode was significantly lower than that of the Bi NSs/CF electrode. This difference was attributed to the advantages of the integrated structure of the Bi NSs/CF material, which does not require electrode binders and benefits from superior conductivity and faster electron transfer rates.

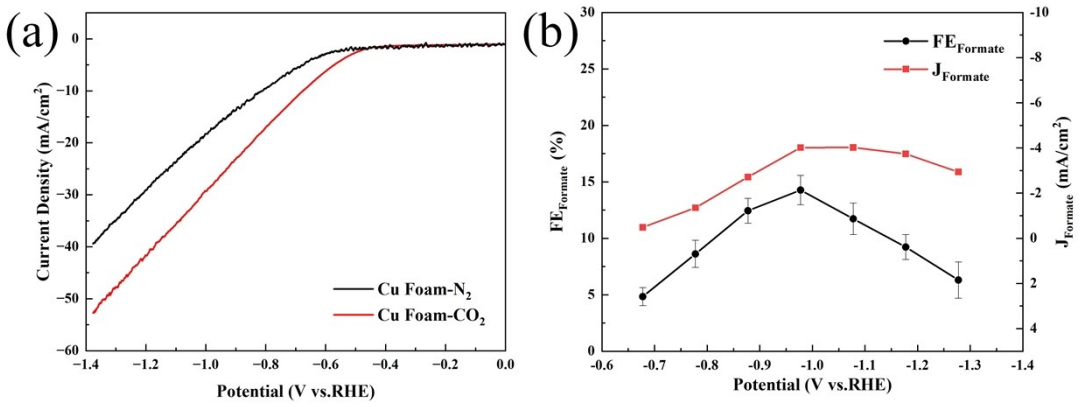

Figure S11. CO_2RR performance of Cu foam.
(a) LSV curves in N_2 or CO_2 atmosphere. (b) Faradaic efficiencies and partial current densities of formate.

Performance tests for CO_2RR were conducted on the Cu foam material, including LSV comparisons in N_2 and CO_2 atmospheres, and experiments to measure the selectivity for formate and formate partial current densities at various applied potentials. The experimental results showed that as the applied potential became more negative, the selectivity of the Cu foam for formate initially increased and then decreased. The maximum value of $FE_{Formate}$ was achieved at -0.98 V, with a value of 14.27%, which was significantly lower than that of Bi NSs/CF ($FE_{Formate}$ = 93.73%, -0.98 V). This indicates that the pure Cu interface does not exhibit excellent CO_2RR activity.

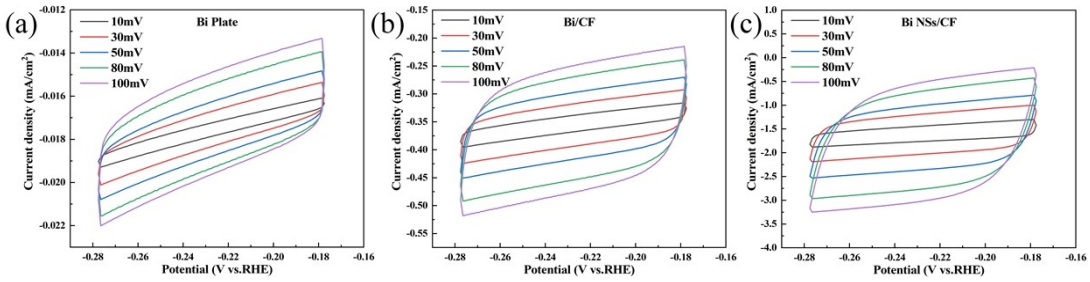

287

288 Figure S12. Cyclic voltammogram (CV) curves of (a) Bi plate, (b) Bi/CF and (c) Bi NSs/CF in
289 CO_2 saturated 0.5 M $KHCO_3$ electrolyte between -0.277 V and -0.177 V vs. RHE.

290

291 Table S2. The corresponding EIS parameters of Bi Plate, Bi/CF and Bi NSs/CF electrodes.

Electrode materials	Bi Plate	Bi/CF	Bi NSs/CF
Rs(Ω)	4.66	4.64	4.71
Rct(Ω)	3.20	2.89	2.53

292

293

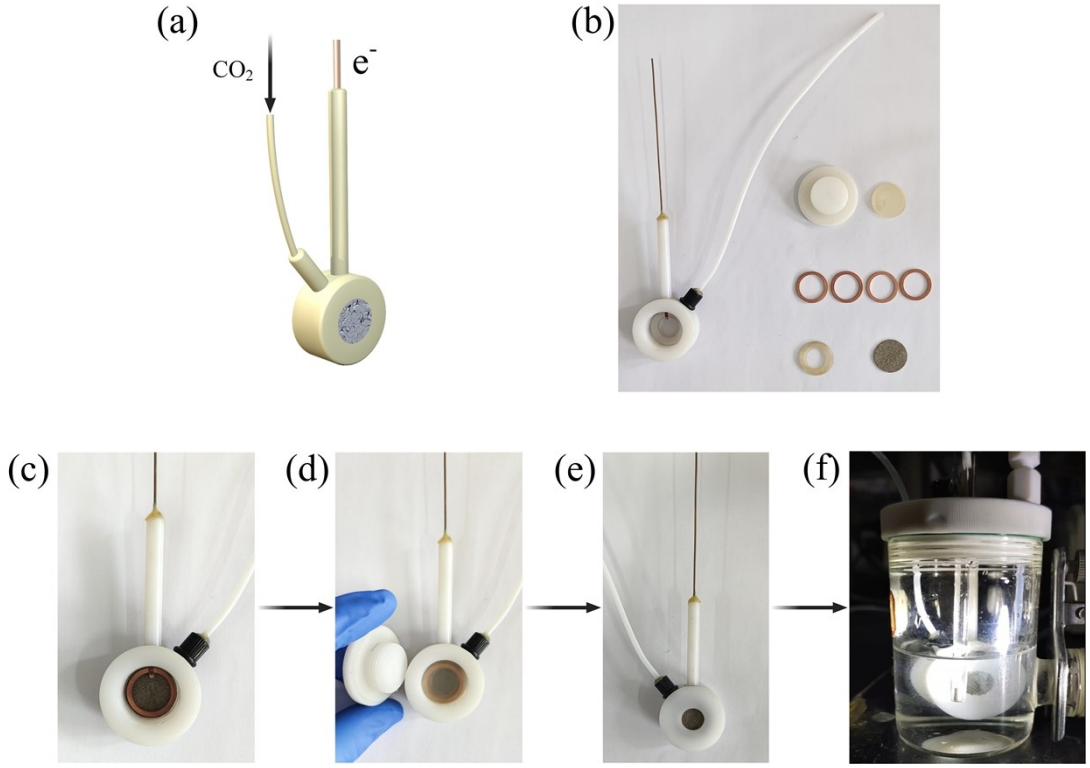

Figure S13. Structure and assembly of the cathode electrode support.
(a) Schematic diagram of the electrode support structure. (b) Physical diagram of disassembled electrode support structure. (c-d) Assembly process of the electrode support.

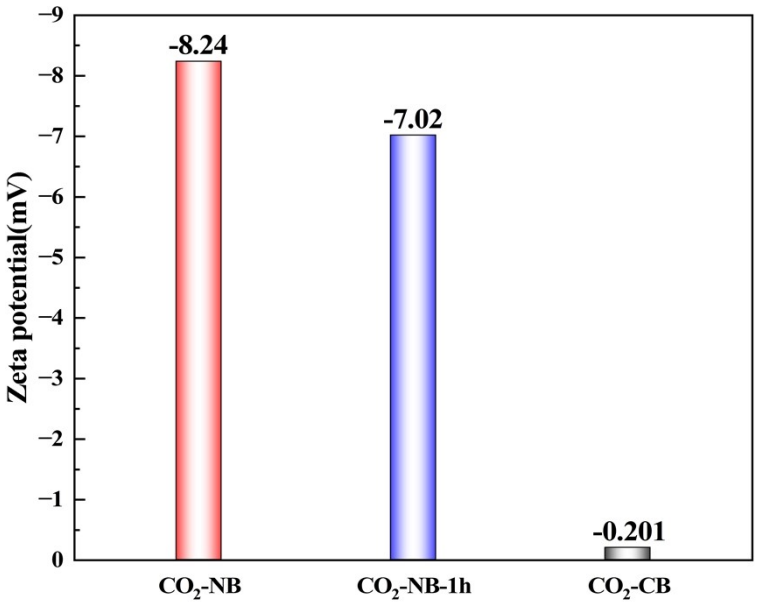

299

300 Figure S14. Zeta potential of fresh nanobubbles (CO_2-NB), nanobubbles after 1 h of participation
301 in the CO_2RR (CO_2-NB-1h), and bubbles of conventional saturated CO_2 (CO_2-CB).

302

303 Table S3. Calculation of CO_2 supply in conventional bubble form and nano-bubble form.

Calculation item	CO_2 supply form	
	Conventional bubbling	NB
CO_2 supply rate (mL/min)	50	800
CO_2 supply per hour (mL)	50*60=3000	800*5=4000
Electrolyte volume (mL)	70	400
Gas-liquid ratio(mL/mL)	3000/70=42.86	4000/40=10
Normalized to the amount of gas required per hour for 100mL electrolyte (mL)	42.86*100=4286	10*100=1000
CO_2 supply per hour (mol/100mL)	4286/1000/22.4=0.1913	1000/1000/22.4=0.0446

304 The conventional CO_2 supply mode adopts the continuous CO_2 bubbling mode,
305 while the NB mode adopts the intermittent working mode and supplies 5 minutes per
306 hour, which can complete the sufficient CO_2 supply. The CO_2 supply in both forms is
307 normalized to the amount of substances that supply CO_2 per hour per 100mL of
308 electrolyte.
309

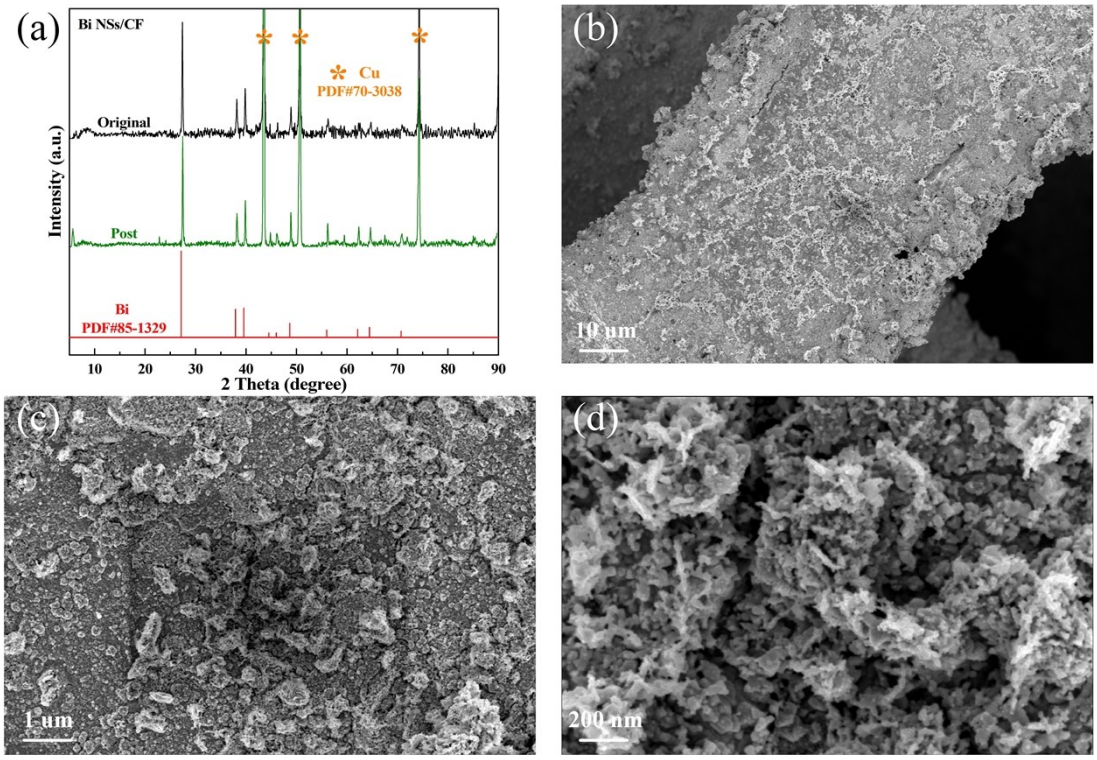

Figure S15. (a) XRD pattern and (b-d) SEM images of Bi NSs/CF obtained after long-term bulk electrolysis.

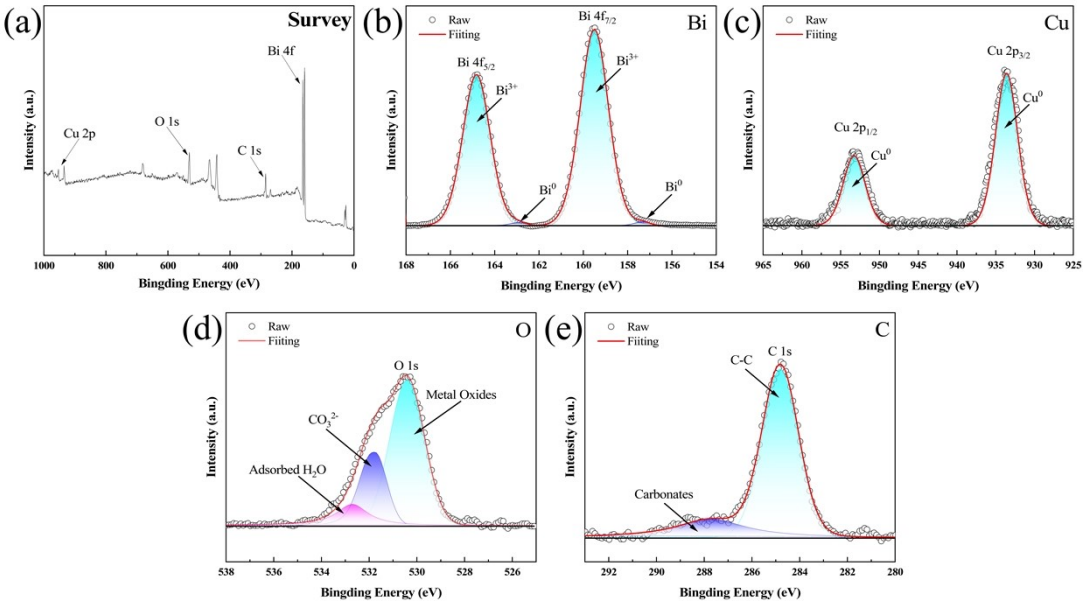

Figure S16. XPS spectra of (a) Bi NSs/CF composite and individual element of (b) Bi, (c) Cu, (d) O and (e) C at high-resolution after long-term bulk electrolysis.

After long-term bulk electrolysis, XPS analysis was performed on Bi NSs/CF to analyze the changes in the valence states of surface elements. From the high-resolution spectrum of Bi (Figure S16b), it was found that the characteristic peaks of Bi^0 at 4f 7/2 and 4f 5/2 were significantly weakened, suggesting a reduction in the content of Bi^0 on the electrode surface. Meanwhile, in the high-resolution O spectrum (Figure S16d), a notable enhancement of the signature peak at 531.7 eV, corresponding to oxygen in carbonate, was observed. Additionally, the characteristic peak observed at 287.72 eV in the high-resolution spectrum of C (Figure S16e) is likely attributable to the carbon in carbonyl (C=O) or carbonate (CO_3^{2-}). Based on these observations, we speculate that after prolonged electrochemical reactions, a compound similar to $Bi_2O_2CO_3$ may have formed on the surface of Bi NSs/CF. Furthermore, no related oxidation peaks were found in the high-resolution spectrum of Cu (Figure S16c).

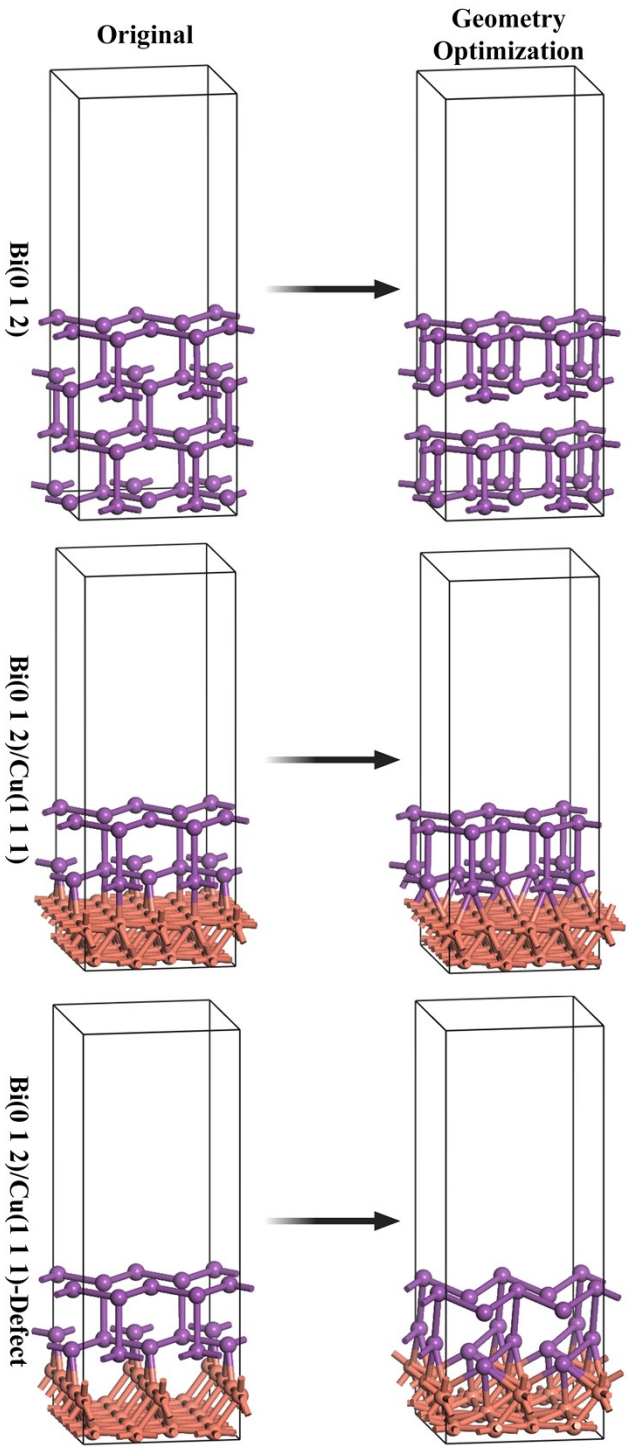

Figure S17. Initial configurations and optimized configurations of Bi(0 1 2), Bi(0 1 2)/Cu(1 1 1) and Bi(0 1 2)/Cu(1 1 1)-Defect structures.

In these structures, the Bi(0 1 2) structure consists of four layers of Bi(0 1 2) crystal planes; the Bi(0 1 2)/Cu(1 1 1) structure comprises two layers of Bi(0 1 2) crystal planes and two layers of Cu(1 1 1) crystal planes; and the Bi(0 1 2)/Cu(1 1 1)-Defect structure is derived from the Bi(0 1 2)/Cu(1 1 1) structure by stripping away part of the atoms from the third layer of the Cu(1 1 1) crystal plane from top to bottom. Structural optimization was carried out on all the structures.

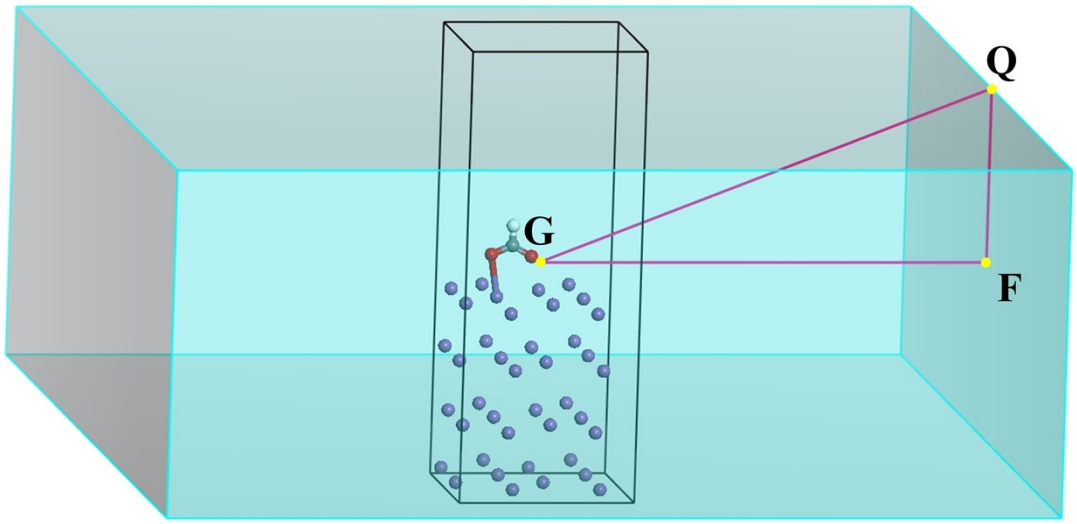

Figure S18. Brillouin zone path.

The path of the Brillouin zone was as follows: it started at point Q (0, 0.5, 0.5), proceeded to point G (0, 0, 0), then moved to point F (0, 0.5, 0), and finally returned to point Q.

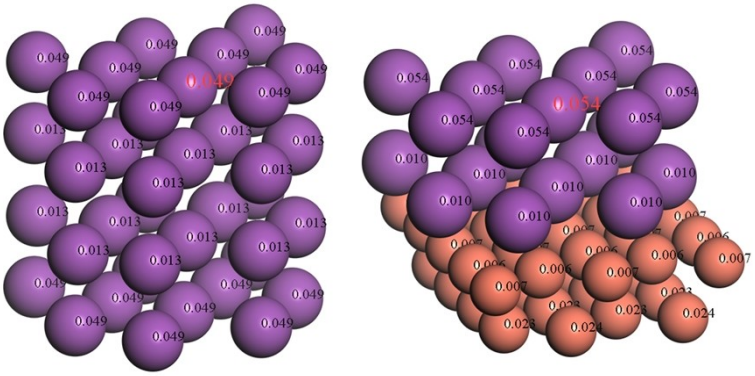

346

347 Figure S19. Distribution of electrophilic attack indices on Bi(0 1 2) and Bi(0 1 2)/Cu(1 1 1).

348

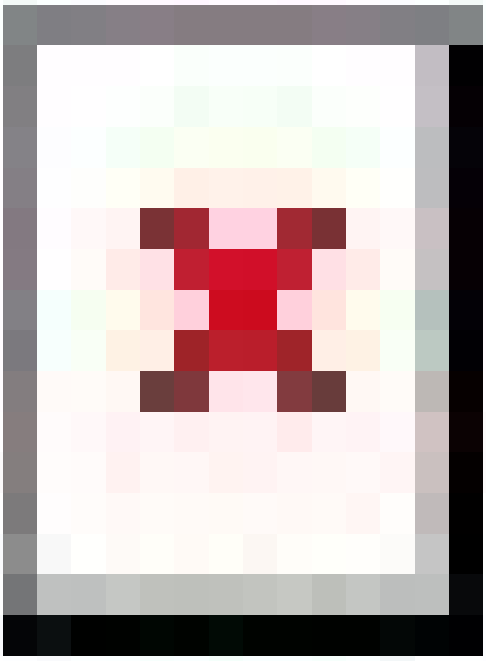

Figure S20. Differential charge density plot of the *OCHO intermediate adsorbed on Bi(0 1 2), Bi(0 1 2)/Cu(1 1 1) and Bi(0 1 2)/Cu(1 1 1)-Defect structures. Red: charge accumulation, blue: charge depletion.

Table S4. Electronic energy (E_{DFT}), zero point energy correction (E_{ZPE}), heat capacity and entropy contribution ($\int$CpdT-TS) in this study.

Species	E_{DFT} (eV)	E_{ZPE} (eV)	$\int$CpdT-TS (eV)
H_2	-31.7451	0.2701	-0.4208
CO_2	-5128.7458	0.3008	-0.5648
HCOOH	-5160.6404	0.8938	-0.7688
H_2O	-2078.4844	0.5682	-0.6016
CO	-3081.2212	0.1323	-0.6110
Bi(0 1 2)	-124872.2568	0	0
Bi(0 1 2)/Cu(1 1 1)	-256221.6609	0	0
Bi(0 1 2)/Cu(1 1 1)-Defect	-207769.6382	0	0
*H on Bi(0 1 2)	-124887.4126	0.1459	-0.0073
*H on Bi(0 1 2)/Cu(1 1 1)	-256236.9266	0.1392	-0.0088
*H on Bi(0 1 2)/Cu(1 1 1)-Defect	-207784.92	0.1499	-0.0106
*OCHO on Bi(0 1 2)	-130016.7336	0.5881	-0.1647
*OCHO on Bi(0 1 2)/Cu(1 1 1)	-261366.2515	0.5966	-0.1564
*OCHO on Bi(0 1 2)/Cu(1 1 1)-Defect	-212914.3013	0.6068	-0.1752
*COOH on Bi(0 1 2)	-130016.1683	0.5997	-0.1516
*COOH on Bi(0 1 2)/Cu(1 1 1)	-261365.7744	0.6017	-0.1851
*COOH on Bi(0 1 2)/Cu(1 1 1)-Defect	-212913.7450	0.6004	-0.1574

Table S5. △G of Reaction Path in this study.

△G of Reaction Path (eV)	Surface		
	Bi(0 1 2)	Bi(0 1 2)/Cu(1 1 1)	Bi(0 1 2)/Cu(1 1 1)-Defect
$H^+ \rightarrow 1/2H_2$	0.9344	0.8194	0.7947
$CO_2 \rightarrow$*OCHO	0.9043	0.8073	0.7261
$CO_2 \rightarrow$HCOOH		0.3902	
$CO_2 \rightarrow$*COOH	1.4943	1.2602	1.2939
$CO_2 \rightarrow$CO		0.6880	

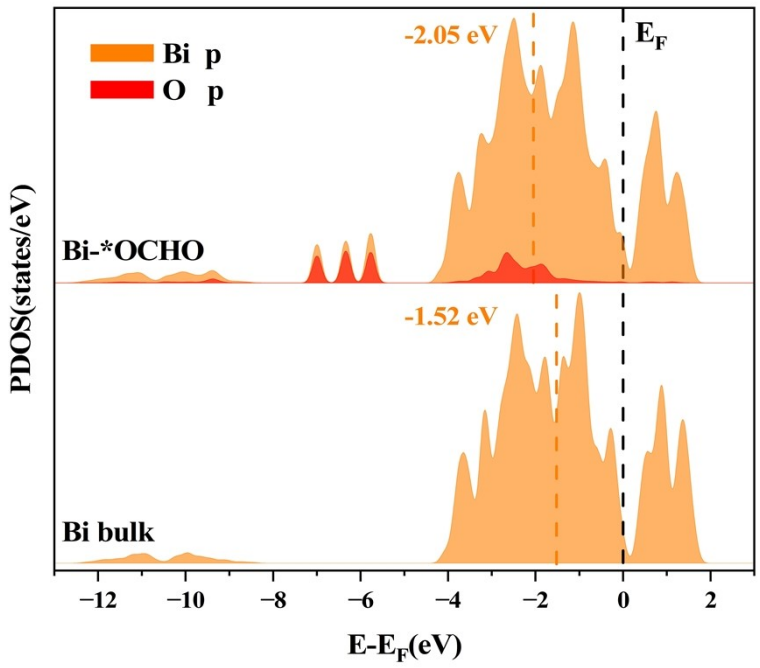

360

361 Figure S21. PDOS of the O p in *OCHO intermediate, the Bi p in Bi(0 1 2) model. The orange
362 dotted lines indicate the center of the p band of Bi, the black dotted lines indicate the Fermi level.
363

Table S6. Comparison of the electrocatalytic activities of Bi NSs/CF with other erstwhile reported Bi-based catalysts for CO_2RR.

Catalyst	Electrolyte	Potential (vs. RHE)	$FE_{Formate}$ (%)	$J_{Formate}$ ($mA \cdot cm^{-2}$)	Cathodic EE (%)	Stability	Ref.
Bi nanoparticles	0.5 M $NaHCO_3$	-1.01	82	54	52.35	40 h	7
Bi NSs-Cu NWs/CC	0.5 M $KHCO_3$	-0.86	87	~4	59.53	8 h	8
Cu mesh@Bi	0.5 M $KHCO_3$	-1.26	~100	68.51	57.43	5 h	9
Nano-sized Bi/copper foil	0.1 M $KHCO_3$	-0.88	91.3	~4	61.88	4 h	10
Bi nanodendrites /Cu foil	0.5 M $KHCO_3$	-0.74	~89	2.7	64.60	12 h	11
Bi dendritic /Cu/Si	0.1 M $KHCO_3$	-0.9	90	~2	60.42	-	12
bismuth oxides	0.5 M $KHCO_3$	-0.9	91	~8	61.09	24 h	13
Bi nanodendrite	0.5 M $NaHCO_3$	-1.13	96.4	15.2	58.41	10 h	14
nano-Bi	0.5 M $KHCO_3$	-0.93	98.4	9.7	65.14	14 h	15
Bi nanosheets	0.1M $KHCO_3$	-1.1	86	16.5	52.78	10 h	16
Bi_2S_3-Bi_2O_3@rGO	0.1 M $KHCO_3$	-0.9	90.1	4	60.49	24 h	17
mpBi	0.5 M $NaHCO_3$	-0.9	99	15	66.46	12 h	18
Untrathin BiNS	0.5 M $NaHCO_3$	-1.06	80	24	49.96	10 h	19
Bi/CeOx	0.2 M Na_2SO_4	-1.2	98	70	57.67	34 h	20
Bi_2O_3-NGQDs	0.5 M $KHCO_3$	-0.9	98.1	18	65.86	15 h	21
Bi NSs/CF	0.5 M $KHCO_3$	-0.98 -1.08 -1.08(NB)	93.73 92.41 95.36	~25.85 ~34.73 ~37.87	60.65 57.21 59.03	- 12 h 72 h	This Work

Note:

cc, carbon cloth.

-, this value is not mentioned in the article.

NB, experiments were carried out under the conditions of CO_2 nanobubbles.

References

1. B. Wulan, L. Zhao, D. Tan, X. Cao, J. Ma and J. Zhang, *Advanced Energy Materials*, 2022, **12**, 2103960.
2. R.-C. Cui, Y.-X. Duan, J.-Y. Xie and Q. Jiang, *Advanced Sustainable Systems*, 2024, **8**, 2300348.
3. J. P. Edwards, Y. Xu, C. M. Gabardo, D. Cao-Thang, J. Li, Z. Qi, A. Ozden, E. H. Sargent and D. Sinton, *Applied Energy*, 2020, **261**, 114305.
4. D. Chen, Z. Chen, L. Chen, Y. Li, S. Xiao and B. Xiao, *Journal of Colloid and Interface Science*, 2022, **607**, 1551-1561.
5. K. Malik, D. Das, D. Mondal, D. Chattopadhyay, A. K. Deb, S. Bandyopadhyay and A. Banerjee, *Journal of Applied Physics*, 2012, **112**, 083706.
6. P. Wang, M. Qiao, Q. Shao, Y. Pi, X. Zhu, Y. Li and X. Huang, *Nat. Commun.*, 2018, **9**, 4933.
7. D. Wu, X. Wang, X.-Z. Fu and J.-L. Luo, *Appl. Catal. B-Environ.*, 2021, **284**, 119723.
8. L. Li, F. Cai, F. Qi and D.-K. Ma, *Journal of Alloys and Compounds*, 2020, **841**, 155789.
9. C. Zhu, Q. Wang and C. Wu, *Journal of Co2 Utilization*, 2020, **36**, 96-104.
10. W. Lv, J. Zhou, J. Bei, R. Zhang, L. Wang, Q. Xu and W. Wang, *Appl. Surf. Sci.*, 2017, **393**, 191-196.
11. J. H. Koh, D. H. Won, T. Eom, N.-K. Kim, K. D. Jung, H. Kim, Y. J. Hwang and B. K. Min, *ACS Catal.*, 2017, **7**, 5071-5077.
12. Z. B. Hoffman, T. S. Gray, Y. Xu, Q. Lin, T. B. Gunnoe and G. Zangari, *ChemSusChem*, 2019, **12**, 231-239.
13. P. Deng, H. Wang, R. Qi, J. Zhu, S. Chen, F. Yang, L. Zhou, K. Qi, H. Liu and B. Y. Xia, *Acs Catalysis*, 2020, **10**, 743-750.
14. H. Zhong, Y. Qiu, T. Zhang, X. Li, H. Zhang and X. Chen, *J. Mater. Chem. A*, 2016, **4**, 13746-13753.
15. Y. Qiu, J. Du, W. Dong, C. Dai and C. Tao, *Journal of Co2 Utilization*, 2017, **20**, 328-335.
16. W. Zhang, Y. Hu, L. Ma, G. Zhu, P. Zhao, X. Xue, R. Chen, S. Yang, J. Ma, J. Liu and Z. Jin, *Nano Energy*, 2018, **53**, 808-816.
17. X. Yang, P. Deng, D. Liu, S. Zhao, D. Li, H. Wu, Y. Ma, B. Y. Xia, M. Li, C. Xiao and S. Ding, *Journal of Materials Chemistry A*, 2020, **8**, 2472-2480.
18. H. Yang, N. Han, J. Deng, J. Wu, Y. Wang, Y. Hu, P. Ding, Y. Li, Y. Li and J. Lu, *Advanced Energy Materials*, 2018, **8**, 1801536.
19. N. Han, Y. Wang, H. Yang, J. Deng, J. Wu, Y. Li and Y. Li, *Nature Communications*, 2018, **9**, 1320.
20. Y.-X. Duan, Y.-T. Zhou, Z. Yu, D.-X. Liu, Z. Wen, J.-M. Yan and Q. Jiang, *Angewandte Chemie-International Edition*, 2021, **60**, 8798-8802.
21. Z. Chen, K. Mou, X. Wang and L. Liu, *Angewandte Chemie-International Edition*, 2018, **57**, 12790-12794.